journal

J. Am. Ceram. Soc., 1–10 (2015)
DOI: 10.1111/jace.13792

Mechanisms of Ytterbium Monosilicate/Mullite/Silicon Coating Failure During Thermal Cycling in Water Vapor

Bradley T. Richards,[‡,†] Matthew R. Begley,[§] and Haydn N.G. Wadley[‡]

[‡]Department of Materials Science and Engineering, University of Virginia, Charlottesville, Virginia 22903

[§]Departments of Mechanical Engineering and Materials, University of California Santa Barbara, Santa Barbara, California 93106

An air plasma spray process has been used to apply a model tri-layer $Yb_2SiO_5/Al_6Si_2O_{13}/Si$ environmental barrier coating system on SiC test coupons. Significant differences in the thermal expansion of the component layers resulted in periodically spaced mud cracks in the Yb_2SiO_5 and $Al_6Si_2O_{13}$ layers. Upon thermal cycling between 1316°C and 110°C in a 90% H_2O/10% O_2 environment flowing at 4.4 cm/s, it was found that partial delamination occurred with the fracture plane located within a thermally grown oxide (TGO) at the $Al_6Si_2O_{13}$–Si interface. Delamination initiated at test coupon edges where the gaseous environment preferentially oxidized the exposed Si bond coat to form β-cristobalite. Simultaneous ingress of the gaseous environment through mud cracks initiated local formation of β-cristobalite (SiO_2), the thickness of which was greatest directly below mud cracks. Upon cooling, cristobalite transformed from the β to α phase with a large, constrained volume contraction that resulted in severe microfracture of the TGO. Continued thermal cycling eventually propagated delamination cracks and caused partial spallation of the coatings. Formation of the cristobalite TGO appears to be the delamination life-determining factor in protective coating systems utilizing a Si bond coat.

I. Introduction

Efforts to improve the fuel efficiency of aero-gas turbine engines are driving increases in gas path temperature throughout the engine.[1–4] Planned increases to the gas temperature in the high-pressure turbine section of engines will require new generations of propulsion materials whose use temperatures exceed the capabilities of current, internally cooled (and thermal barrier coating protected) superalloy structures. Ceramic matrix composites are the favored replacement since they have greater fracture resistance than monolithic ceramics. Those based on SiC fibers coated with BN to create weak interfaces with SiC matrices (resulting in a rising R curve toughening response) appear the most promising.[5–11]

While SiC_f/SiC_m composites provide the high-temperature mechanical properties needed for engine applications, they suffer from rapid recession[12–16] as well as embrittlement and pesting[17–22] in the high-pressure gas turbine environment. Recession originates from water vapor volatilization of the normally protective silica scale,[12–16] and embrittlement compromises the mechanical performance. Environmental barrier coatings (EBCs) that inhibit oxidizer reaction with the SiC component are therefore a critical issue for future engine development.

Numerous EBC concepts have been proposed, but recent reviews have shown many systems suffer from a variety of deficiencies.[23–30] A tri-layer coating consisting of a Si bond coat, an $Al_6Si_2O_{13}$ intermediate layer, and a low steam volatility rare-earth (RE) silicate topcoat has been investigated as a promising system.[23,27,31] The Si bond coat applied to the SiC substrate serves as a cation reservoir to prevent oxidation and volatilization of SiC. An alumino-silicate (3:2 mullite-$Al_6Si_2O_{13}$) layer above the bond coat is used to impede the diffusion of oxidizers to the bond coat. This two-layer system is then protected from volatilization by a RE silicate topcoat which has low volatility. The use of an intermediate $Al_6Si_2O_{13}$ layer is also thought to inhibit reactions between silicon and rare-earth silicates.[23]

This tri-layer RE coating architecture was first proposed in the mid 2000s,[23] and a variant using a Yb_2SiO_5 topcoat has been recently deposited using air plasma spray (APS) techniques.[31] While Yb_2SiO_5 has a very high silicon volatility resistance,[32] it has a relatively high coefficient of thermal expansion (CTE)[27,31] compared to that of the Si bond coat and SiC substrate. The difference in CTE causes mud cracking of the coating, with cracks terminating at the Si bond coat.[27,29,31] Nonetheless, the $Yb_2SiO_5/Al_6Si_2O_{13}/Si$ system has been proposed as one of the most promising among the tri-layer RE silicate systems due to its thermochemical stability at high temperatures, the stability of Yb_2SiO_5 in a steam environment, and reported adherence and durability during steam cycling.[23,27]

While the thermochemical compatibility and stability of numerous EBC concepts have been studied extensively,[23,25–27,29,30,33–37] there have been no published reports analyzing the thermomechanical damage mechanisms experienced during steam cycling of thermochemically stable plasma-sprayed RE silicate EBC systems. Here, a steam cycling study has been performed for a tri-layer $Yb_2SiO_5/Al_6Si_2O_{13}/Si$ (ytterbium monosilicate/mullite/silicon) system whose APS deposition and coating microstructure have been recently described,[31] and the evolution of damage and mechanisms of failure during steam cycling are investigated.

II. Experimental Procedure

(1) Coating Deposition

Three-layer $Yb_2SiO_5/Al_6Si_2O_{13}/Si$ coatings were deposited onto (grit blast) roughened 25.4 mm × 12.7 mm × 3.2 mm α-SiC Hexoloy® (Saint Gobain Ceramics, Niagara Falls, NY) substrates using an APS deposition approach described by Richards and Wadley.[18] The Si layer was deposited with the substrate at ambient temperature. The $Al_6Si_2O_{13}$ and then Yb_2SiO_5 layers were deposited on the Si-coated substrates in a furnace held at 1200°C. The structure of the coated samples is schematically illustrated in Fig. 1. Only

J. L. Smialek—contributing editor

Manuscript No. 36176. Received January 1, 2015; approved June 22, 2015.
†Author to whom correspondence should be addressed. e-mail:btr4we@virginia.edu

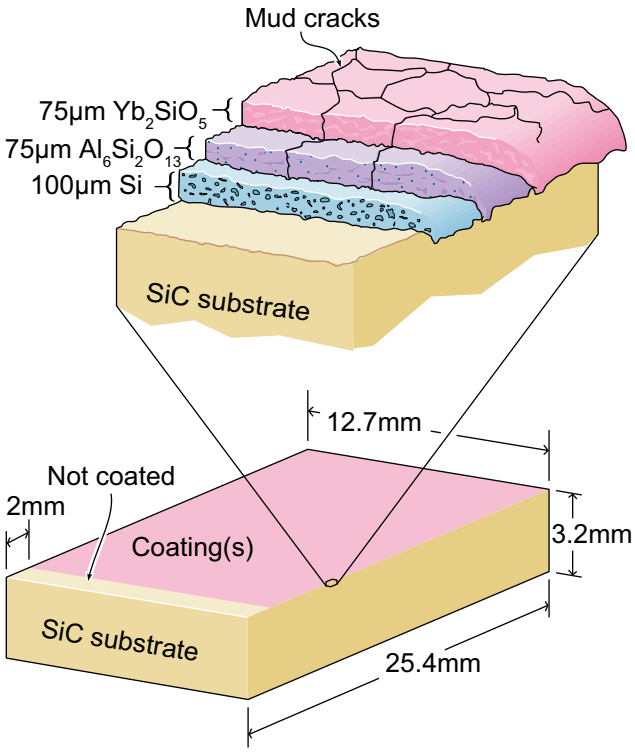

Fig. 1. Schematic illustration of the tri-layer EBC covered SiC samples showing the coating structure and side edge coverage of the substrate.

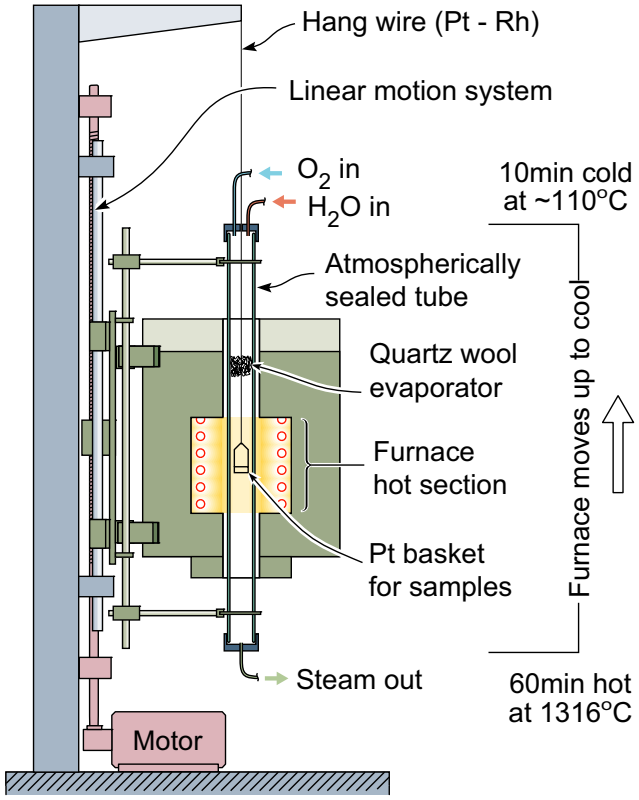

Fig. 2. Schematic illustration of the steam cycling furnace in the configuration that subjected the samples to the hot part of a steam cycle (60 min at 1316°C). The furnace was then translated vertically while maintaining the sample stationary, thereby removing the sample from the furnace hot zone and subjecting it to the cold part of a steam cycle (10 min at 110°C).

one surface of the substrate was coated, and the side edges were slightly over-sprayed. A 2 mm-wide strip of the sample surface was left uncoated due to the fixture used for deposition. The nominal thickness of the Yb_2SiO_5 and $Al_6Si_2O_{13}$ layers was 75 μm, whereas that of the Si bond coat was 100 μm. However, considerable variability in layer thickness was observed within and between specimens due to fluctuation of the powder particle feed rate and variation in particle temperature during propagation within the plasma plume over the long spray distance.[31]

(2) Steam Furnace Cycling

After deposition, the coated samples were "stabilization" annealed at 1300°C in laboratory air for 20 h, consistent with prior EBC testing.[23,27,29] They were then thermally cycled in a steam cycling furnace in a flowing, atmospheric pressure, 90% H_2O/10% O_2 gas environment with a flow velocity of 4.4 cm/s (volumetric flow rate of 4.1 slm), Fig. 2. When the steam furnace was in its raised (cold) configuration, the gas temperature at the sample location was 110°C (thereby avoiding steam condensation). In the hot configuration, the sample temperature was measured to be 1316°C by reference thermocouple. These testing conditions are similar to those used in prior EBC research,[23] and approximate the H_2O partial pressure during lean combustion at a pressure of ~10 atm. The samples were examined visually before testing, after 50, 100 and then every 100 cycles thereafter to determine sample failure defined as coating spallation on any part of the test sample.

(3) Coating Characterization

The steam cycled samples were sectioned and polished, and examined with a scanning electron microscope (Quanta 650 FE-SEM; FEI, Hillsboro, OR) operating in the backscattered electron (BSE) mode. Images are collected under low-vacuum conditions. A gamma correction was applied to images to enable simultaneous visualization of Yb and non-Yb containing materials. Elemental mapping by Energy Dispersive Spectroscopy (EDS-X-Max^N 150 SDD, Oxford Instruments, Concord, MA) was also used. The EDS spectra were captured using a 20 kV accelerating voltage to identify Yb by its L lines and were not standardized.

Raman Spectroscopy was performed using an inVia (Renishaw, Hoffman Estates, IL) microscope to identify bond coat oxidation phases and reaction products in steam cycled coatings. The Raman analyses were performed using a 50× lens with a numerical aperture of 0.5. An argon-ion laser (wavelength of 488 nm) was used for incident illumination of the sample. Approximately 99% of the Gaussian distributed incident light of the source resided within a 1 μm diameter circle, resulting in a spatial resolution of approximately 1 μm.

(4) Thermomechanical Analysis

Thermomechanical analyses of stress states and strain energy release rates (ERR) for debonding of the elastic coating layers were calculated using the LayerSlayer[38] software package. All strain ERR calculations presented are for a system whose layers remained elastic throughout cooling, under the assumption that all layers are in their stress-free state at the annealing temperature of 1300°C. The calculation ignores stress relief by mechanisms such as mud cracking or creep. The thermophysical properties and residual stresses calculated for this elastic coating—substrate system after cooling from the stabilization (stress free) annealing temperature of 1300°C are summarized in Table I and agree well with previous estimates.[31,39,40,40–49]

III. Results

Eight substrates had coatings deposited upon them. One sample was used for as-deposited and annealed microstructural

Table I. Thermophysical Properties of EBC System Components

Material	CTE ($\times 10^6$ °C^{-1})	Young's modulus (GPa)	Poisson ratio ν	Thermal stress (MPa)†	Layer thickness	Application
Yb_2SiO_5	7.5[31]	172[31]	0.27§	840	75 μm	Topcoat
E_{APS}‡		86		425		
Mullite	5.3[41]	220[42]	0.28[43]	215	75 μm	Diffusion barrier
E_{APS}‡		110		110		
Cristobalite-α	30¶	65[44]	−0.164[46]	4350	0–150 μm	Oxidation product
Cristobalite-β	3.1[49]	70‖	−0.042[48]			
Si	4.1[42]	163[49]	0.223[49]	−180	100 μm	Bond coat
E_{APS}‡		16		−17		
SiC (α)	4.67	430	0.14	−55	3.2 mm	Substrate
				−34		

†Calculated at 20°C after cooling from stress free condition at 1300°C with LayerSlayer.
‡Assumed 50% reduction in elastic modulus for APS Yb_2SiO_5 and $Al_6Si_2O_{13}$ and 90% reduced elastic modulus for porous APS Si.
§Based on $Y_2Si_2O_7$.[39]
¶Average of values reported on the 20°C–200°C interval.[44,45]
‖Based on Young's modulus ratio of α and β quartz[40] and α cristobalite.

analysis, one sample delaminated upon cooling from deposition and a second delaminated upon cooling from annealing. Both delamination types were investigated by SEM and found to have occurred at the Si–SiC interface. The remaining five coated samples were thermally cycled in the steam cycling apparatus shown in Fig. 2. Spallation failure was observed in the cycled coatings at 50, 200, 400 (2), and 600 cycles.

(1) Coating Structure

Figure 3 shows BSE mode SEM micrographs of a part of the coating–substrate system after stabilization annealing. The white arrows in Fig. 3(a) indicate the locations of mud cracks in the Yb_2SiO_5 layer. Many of these also penetrated the $Al_6Si_2O_{13}$ layer, Fig. 3(b) but were arrested near the $Al_6Si_2O_{13}$–Si interface, Fig. 3(c). Examination of the calculated residual stress states in the coated system, Table I, indicates that the higher CTE of the Yb_2SiO_5 (and to lesser extent the $Al_6Si_2O_{13}$) layer resulted in tensile residual stresses. The residual stresses have been bounded by performing the calculations using two sets of elastic moduli. The first used the elastic moduli typical of fully dense material, and resulted in high tensile stresses in the Yb_2SiO_5 and $Al_6Si_2O_{13}$ layers and a compressive stress in the Si bond coat. The second used 50% reduced elastic moduli to approximate the properties of the APS deposited Yb_2SiO_5 and $Al_6Si_2O_{13}$ layers. It also used an elastic modulus for the highly porous (calculated to be in the range of 20% porosity)[31] Si bond coat that was 1/10th that of the solid material. These reduced moduli are consistent with those experimentally observed for APS materials of comparable porosity.[50–58] They resulted in lower tensile stresses in the Yb_2SiO_5 and $Al_6Si_2O_{13}$ layers and a substantially smaller compressive stress in the Si bond coat. In either case, the calculated stresses are consistent with the mud cracking observed. The average mud crack spacing was found to be ~280 μm, consistent with prior work.[31]

The light and dark contrast features evident in the Yb_2SiO_5 coating layer, Fig. 3, are a manifestation of silicon evaporation from some of the (originally stoichiometric composition) powder particles during APS processing.[31] The lighter contrast regions correspond to solidified particles

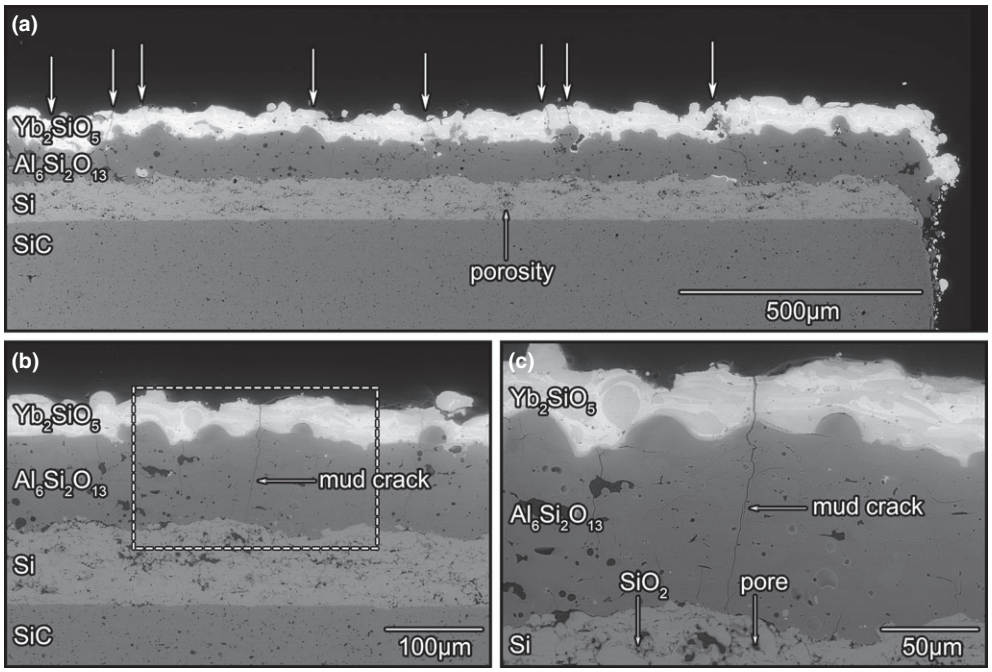

Fig. 3. (a) Low magnification BSE mode SEM image of the 1300°C annealed EBC with mud cracks indicated by arrows. (b) Shows a higher magnification view of the coating in a region where a mud crack penetrated the ytterbium monosilicate and mullite layers. (c) A high magnification view of the dashed box area in (b) showing arrest of the mud crack at the mullite–silicon bond coat interface.

containing a lower silicon fraction. During their solidification, this resulted in the formation of a two-phase $Yb_2SiO_5 + Yb_2O_3$ solidified splat. It is worth noting that since the CTE and elastic modulus of Yb_2SiO_5 and Yb_2O_3 are similar,[31] such silicon loss is not anticipated to significantly affect the thermomechanical response of the topcoat.

Figure 3(a) shows that significant variability in the thickness of the coating layers (especially the top two layers) resulted from the spray process implemented here. It can also be seen that the Yb_2SiO_5 and $Al_6Si_2O_{13}$ layers failed to fully cover the Si bond coat at the coating edge, despite intentional overspray. While this could generally be resolved by changing the angle of deposition of these two layers, the high-temperature furnace prevented spraying at an angle.

During the spray deposition process, the temperature and size of the silicon droplets that impacted the SiC substrate varied considerably. This resulted in a porous Si bond coat and significant variability in the adhesion of the interface between the grit blasted SiC and the Si bond coat. Figure 4 shows BSE micrographs of the Si bond coat—SiC interface at two different locations in an annealed sample. In some regions of the interface, Fig. 4(a), silica formation and substantial porosity were observed. The silica formation resulted from oxygen entrainment in the plasma and reaction during the long standoff spray deposition, and penetration through interconnected pore paths in deposited coatings during annealing. The concentration of these defects varied greatly within specimens. Figure 4(b) shows an interface from a region where these defects were much less prevalent. Those specimens that spalled before steam cycling were found to have spalled at the Si–SiC interface, from regions containing these defects identified in Fig. 4.

(2) Steam Cycling Response

The samples that had very short delamination lifetimes (<200 steam cycles) all delaminated at the Si–SiC interface. Figure 5(a) shows a photograph of a coated substrate that had the shortest delamination lifetime (less than 50 steam cycles). A photograph taken after its delamination failure is shown in Fig. 5(b). It is evident that failure began at the left edge on this sample and progressed inward toward the center of the coating. Figure 5(c) shows a cross-sectional image taken near the side of the sample at the location indicated by a red vertical bar in Fig. 5(b). While the coating remained adherent, it was clear that delamination had initiated at the Si–SiC interface. The crack opening displacement at the edge of the sample indicates the presence of a bending moment on the coating that is consistent with the higher CTE of layers further from the mid-plane of the coating.

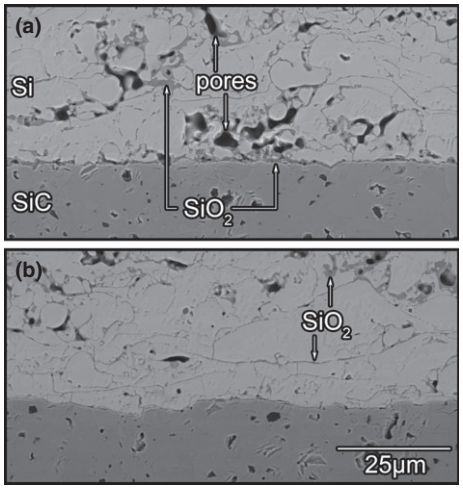

Fig. 4. The Si–SiC interface of (a) an annealed sample in a region of relatively poor adherence with oxidized pore structures and poor interfacial bonding and (b) an interfacial region of higher quality in the same annealed specimen.

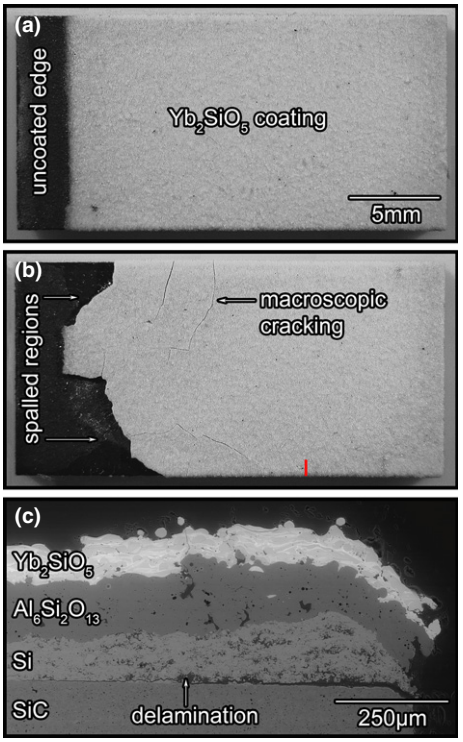

Fig. 5. Images of an EBC covered sample. (a) Optical image of top surface after annealing. (b) Optical image of the top surface of the same sample after it had delaminated following 50 steam cycles at 1316°C. (c) SEM cross section (in BSE mode) of the delaminated sample shown in (b). The red bar in (b) indicates the location of the cross section shown in (c).

Delamination after a few steam cycles (and immediately after deposition and cooling from annealing) appears to be a consequence of the large thermal residual stress in the coating system (as outlined in Table I) acting in combination with insufficient Si–SiC interfacial adhesion. This is consistent with deposition conditions for these samples that resulted in interface sections such as that shown in Fig. 4(a). No delamination of this character was evident in coatings with a steam cycling lifetime in excess of 200 steam cycles.

An example of the failure mode of the sample that was most delamination resistant (600 steam cycles to failure) is shown in Fig. 6. This figure shows cross-sectional BSE images of the coating at various distances from the edge of the sample. Examination of these serial coating sections indicates that coating damage occurred at the $Al_6Si_2O_{13}$–Si interface and was greatest near the coating edges, Fig. 6(a). A very thick porous and cracked TGO layer had formed on the Si bond coat. The TGO layer thickness increased toward the sides of the coating, and had microcracked and suffered a mixture of thermomechanical and environmental damage leaving large, interconnected voids at the $Al_6Si_2O_{13}$–Si interface. This damage decreased toward the interior of the sample, Figs. 8(b) and (c). Figure 8(c), near the center of the coating, shows that cavities had been created in the TGO at the base of mud cracks. Analysis of many sample sections indicated that such cavities were present at the bottom of all mud cracks. They were extended horizontally along the $Al_6Si_2O_{13}$–TGO interface, and had the greatest thickness of TGO below them. The cavity edges appeared sharp and were connected with crack network within the TGO layer.

A higher magnification image of the TGO region is compared with EDS mapping in Fig. 7. It is apparent that the microfracture was contained within the TGO scale that

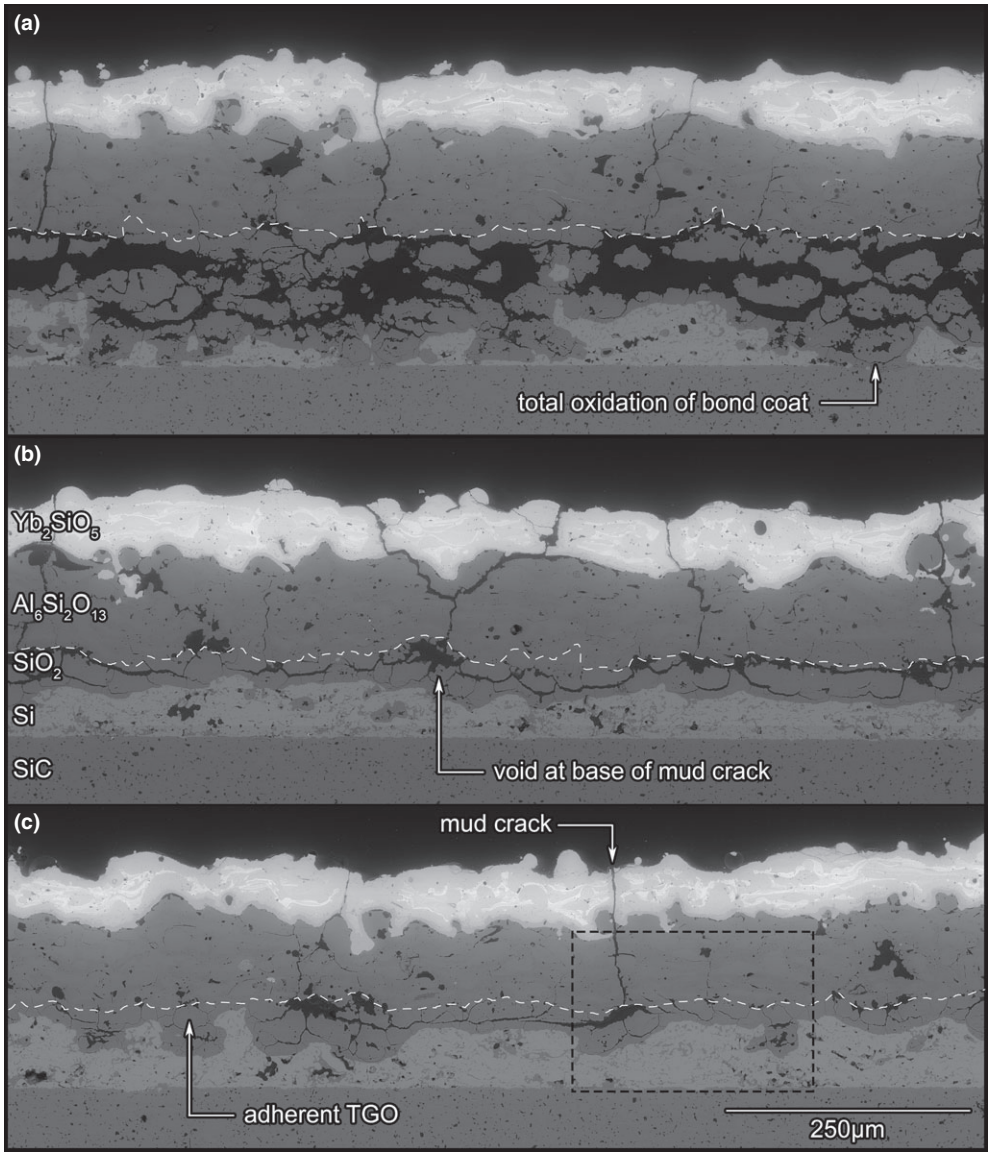

Fig. 6. Cross-sectional BSE micrographs of the same failed coating after 600 1-h steam cycles at 1316°C with serial sections at (a) 1 mm, (b) 3 mm, and (c) 5 mm from the coating edge. The dashed white line shows the TGO-mullite interface. The boxed section in (c) indicates the region subjected to compositional analysis.

grew on the Si bond coat at the original $Al_6Si_2O_{13}$–Si interface. Semiquantitative EDS point analyses of the TGO indicated that it contained only Si and O with a composition consistent with SiO_2. In addition to the formation of the TGO, considerable internal oxidation of the Si bond coat is evident. This is consistent with an interconnected (open) pore structure whose interior surfaces were oxidized during annealing and subsequent steam cycling.

The TGO has been analyzed using Raman spectroscopy, and the ambient temperature phase identified to be α (low) cristobalite based on the presence of spectral peaks with wave numbers of 230 and 416 cm^{-1},[59–61] Fig. 8. The presence of the silicon peak at a wave number of 520 cm^{-1} indicates that Si–Si bonding was sampled by the probe. The observed intensity of this peak is very low compared to the intensity for pure silicon, and may be due to retained silicon in the oxide. Raman analyses across the width of the coating (Fig. 8) all indicated the TGO to be α cristobalite; no vitreous SiO_2 was detected. While this does not preclude the presence of vitreous silica, it indicates that if a vitreous phase existed its thickness was less than the ~1 μm diameter laser probe. The presence of α (low) cristobalite at ambient temperature implies that β (high) cristobalite was formed during high-temperature H_2O/O_2 exposure and then underwent a phase transformation to the α phase during cooling. Such a phase change typically commences at ~220°C during the cooling of β-cristobalite and is complete by ~200°C.[44,61–63] The variation in background may result from the incorporation of hydroxyl groups within the silica.[64]

Modest microstructural changes occurred within the Yb_2SiO_5 and $Al_6Si_2O_{13}$ layers during steam cycling, Fig. 9. After 200 steam cycles equiaxed microcracking of the Yb_2SiO_5 phase in the topcoat was observed, Fig. 9(a). In the $Al_6Si_2O_{13}$ layer, increased precipitation of Al_2O_3 aggregates and coarsening into larger plates was observed, Fig. 9(b). The presence of such plates has been previously identified in this system.[31] No evidence of surface volatilization of silica was observed. Steam cycling of the coating system resulted in the formation of a reaction product between the Yb_2SiO_5 and $Al_6Si_2O_{13}$ layers, Fig. 10. The semiquantitative EDS-measured composition of this reaction product ranged between 11–12 at.% Yb, 11–20 at.% Al, 14–20 at.% Si, and 56–57 at.% O. Its thickness varied considerably and exceeded 5 μm in some locations. The varying Al and Si contents indicate that the compound has a broad phase field. No cracking of the reaction product was observed, but

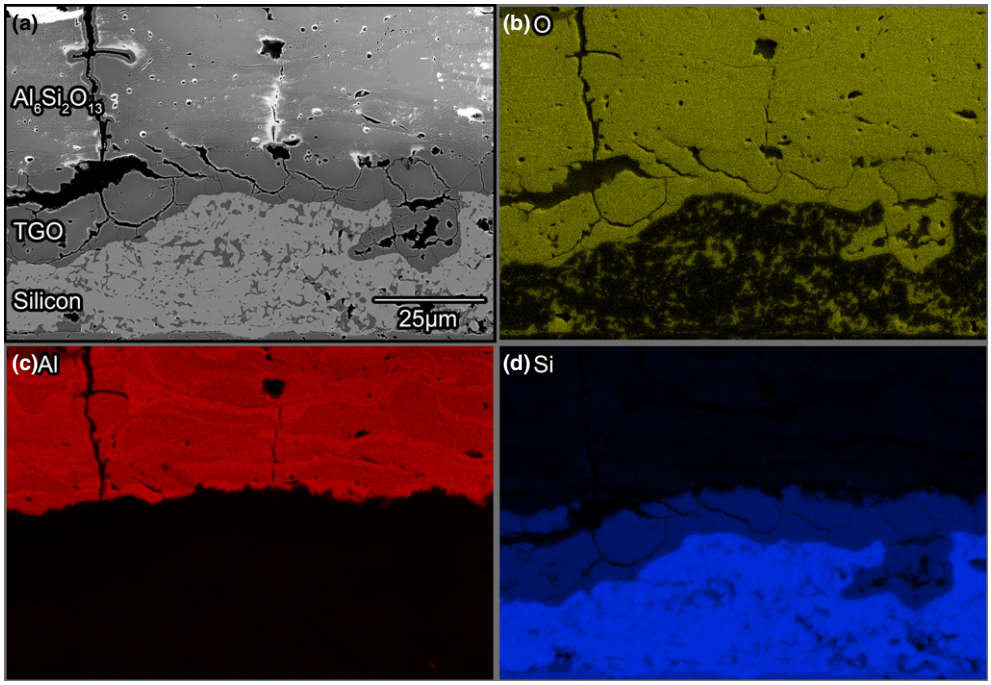

Fig. 7. (a) A SEM image taken in BSE mode of a mud crack root intersection with an adherent silica TGO–$Al_6Si_2O_{13}$ interface as identified in Fig. 6(c). (b) An oxygen, (c) aluminum, and (d) silicon dot map of the same region.

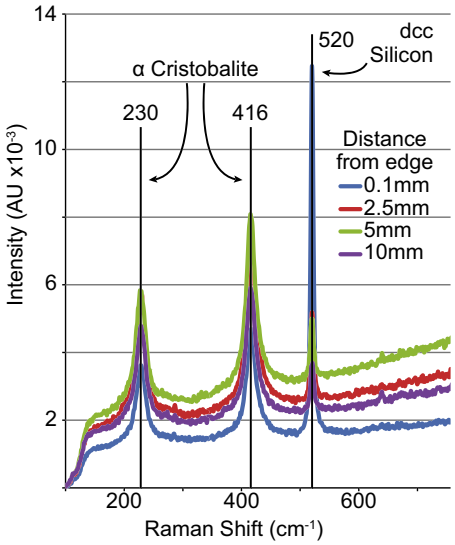

Fig. 8. Raman spectra from the thermally grown (silica) oxide at the Si–mullite interface as a function of distance from the edge of the coated sample.

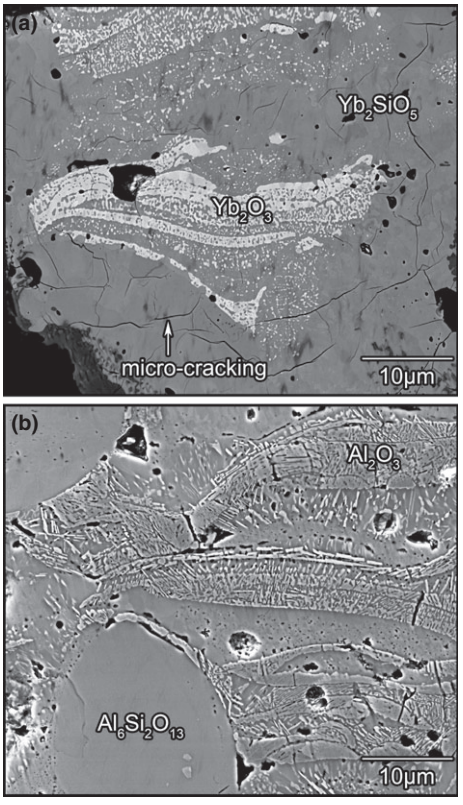

Fig. 9. High magnification BSE mode SEM images of (a) ytterbium monosilicate and (b) mullite layers after a 200 steam cycle exposure.

porosity was present at the interface between the Yb–Al–Si–O reaction product and $Al_6Si_2O_{13}$ layer. Raman analyses of this reaction product, Fig. 11, indicated that it was crystalline and shared many of the atomic bonding configurations present in Yb_2SiO_5, though several additional peaks were also present in the spectra. Raman spectra of the Yb–Al–Si–O system are not published so this reaction product could not be identified by this method.

IV. Calculated Stress States and Energy Release Rates

The mechanical properties and calculated thermal residual stresses for the EBC system of Fig. 1 are presented in Table I. Some explanation is merited for the stress states and ERRs calculated for systems including cristobalite. It was assumed that oxidation grows a pure β cristobalite scale under stress free conditions at the steam cycling temperature of 1316°C. Upon cooling, strain is generated by the thermal contraction of the layers. Inelastic deformation during cooling is neglected, such that the present calculations correspond to an upper bound on the strain energy contained in the layers (and therefore on the ERR). At 220°C an inversion-type phase transformation occurs in cristobalite [i.e., β (high)

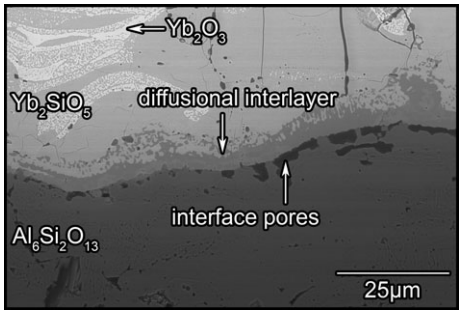

Fig. 10. SEM micrograph (in BSE mode) of the interface between the ytterbium monosilicate and mullite layers in a sample that delaminated after 600 steam cycles at 1316°C. Note the formation of an approximately 5-μm-thick reaction product between the two layers and interfacial pores created by the interdiffusion reaction.

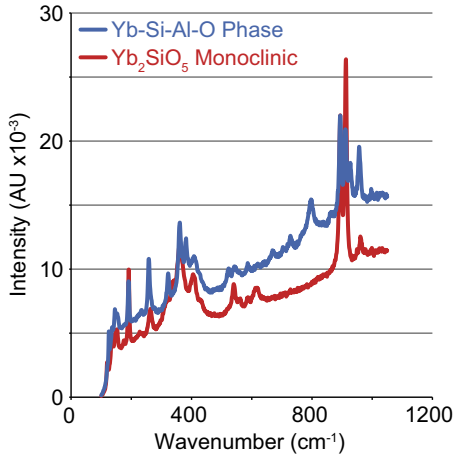

Fig. 11. Raman spectra of the Yb–Si–Al–O reaction product formed at the Yb_2SiO_5–$Al_6Si_2O_{13}$ interface in Fig. 10 and a reference pattern for the Yb_2SiO_5 coating.

transforms to α (low)], with a volume reduction of 4.5% (an average of previously reported experimental values).[44,63] The system is then further cooled with additional strain generated according to the CTE of α cristobalite and the other layers of the system. The cristobalite is assumed to be constrained in the plane of the coating by the surrounding layers, and stresses are based upon the misfit strains, consisting of contributions from thermal and transformation strains. The resulting thermal residual stress at 20°C within the cristobalite layer was greater than 4 GPa, assuming no cracking or strain relaxation occurred. Clearly, the large elastic strain energy generated by this phase transformation is a potent driving force for permanent deformation.

The ERR for delamination at the various interfaces in the system both before and after a 20-μm-thick thermally grown SiO_2 scale had formed at the $Al_6Si_2O_{13}$–Si interface have been calculated as a function of temperature assuming plane-strain constraint, and are shown in Figure 12. The conversion of pure Si to SiO_2 is theoretically accompanied by a 110%–120% molar volume increase (depending upon the molar volumes used), but for the case considered here it is assumed that some volatility occurred such that the actual volume increase was 100%, corresponding to a molar volume ratio of 2. The calculations used either the solid elastic modulus for the APS deposited layers [Figs. 12(a)–(c)] or reduced elastic modulus value [Figs. 12(d)–(f), Table I] to account for the compliance introduced by the APS structure. Figure 12(a) shows that when no TGO was present the ERRs of all three interfaces were very similar in magnitude. However, the ERR at interfaces below the TGO were increased considerably when the α-cristobalite TGO was present, Fig. 12(b). Figure 12(c) shows the effect of a 50% reduced elastic modulus for the SiO_2 layer to approximate the consequences of its dense crack network: this reduced the magnitude of the ERR for delamination at interfaces below the TGO by ~50%, but did not change the trends.

V. Discussion

High-temperature APS deposition of a $Yb_2SiO_5/Al_6Si_2O_{13}$/Si tri-layer EBC on a SiC substrate results in the development of substantial stored elastic strain energy in the coating system after cooling, Figs. 12(a)–(f). It is noted that the ERR for delamination exceeds the toughness of oxide ceramics, which lie in the range 1–50 N/m (roughly equivalent to 0.1–10 MPa·m$^{1/2}$).[65] By comparing Figs. 12(a), (b), (d), and (e) it can be seen that the ERR for interface delamination increased considerably when cristobalite was present above the delaminating interface. Comparison of Figs. 12(b), (c), (e) (f) also show that the increase in ERR was strongly related to the effective modulus of the cracked TGO. The early delamination failures of coatings upon cooling are all consistent with a thermomechanical stress-driven failure mechanism at the Si–SiC interface, which initiated at the stress concentration present at the coating edge[66] and acted in conjunction with insufficient adhesion at the Si–SiC interface.

It is noted again that the neglect of plastic flow (creep) during cooling implies that the ERR estimates are upper bounds. In addition, deformation mechanisms such as the observed channel (mud) cracking, microcracking of the TGO, and other microcracking would all considerably reduce the strain energy available to drive delamination cracking in the cooled state. Analysis of these effects is complicated, and has not been attempted. As shown in Fig. 12, the effect of reduced coating moduli (to account for porosity) and cristobalite modulus (to account for microcracking) on the ERR behavior has been subjected to preliminary investigation. The calculations indicate that the ERR scales approximately linearly with the coating layer modulus. These calculations also indicate that microcracking of the TGO considerably reduces the ERR for delamination.

In those coatings where the Si–SiC interface adhesion was sufficient to avoid early failure, coating delamination occurred by a combination of thermomechanical and environmental effects. A schematic illustration of the damage mechanisms is shown in Fig. 13. After the stabilization annealing treatment, the CTE mismatch between the coating layers and the substrate resulted in a large tensile residual stress in the Yb_2SiO_5 layer. A smaller tensile stress was also formed in the $Al_6Si_2O_{13}$ layer, Table I and Fig. 13(a). These stresses varied considerably based upon the elastic moduli used for their calculation, but were substantial in either case. The tensile stresses resulted in the formation of mud cracks, which were arrested upon encountering the Si bond coat. At ambient temperature, the faces of these mud cracks were quite widely separated in the Yb_2SiO_5 layer.

Upon heating to 1316°C in the steam cycling furnace, the primary damage mechanism became environmental: even though the mud crack opening displacement was greatly reduced by thermal expansion, the gaseous environment permeated the mud crack network and began to oxidize the Si bond coat, forming a β-cristobalite TGO at the root of the mud cracks, Fig. 13(b). Cristobalite has previously been observed in silica scales formed above 1200°C during exposure to H_2O, with a prevalence that increases with temperature and H_2O concentration.[12,67,68] Some volatilization may also occur through the reaction of silica with water vapor,[12–14] but this will be inhibited by the need for diffusive transport of H_2O and $Si(OH)_4$ through the crack network between the TGO and the external environment.

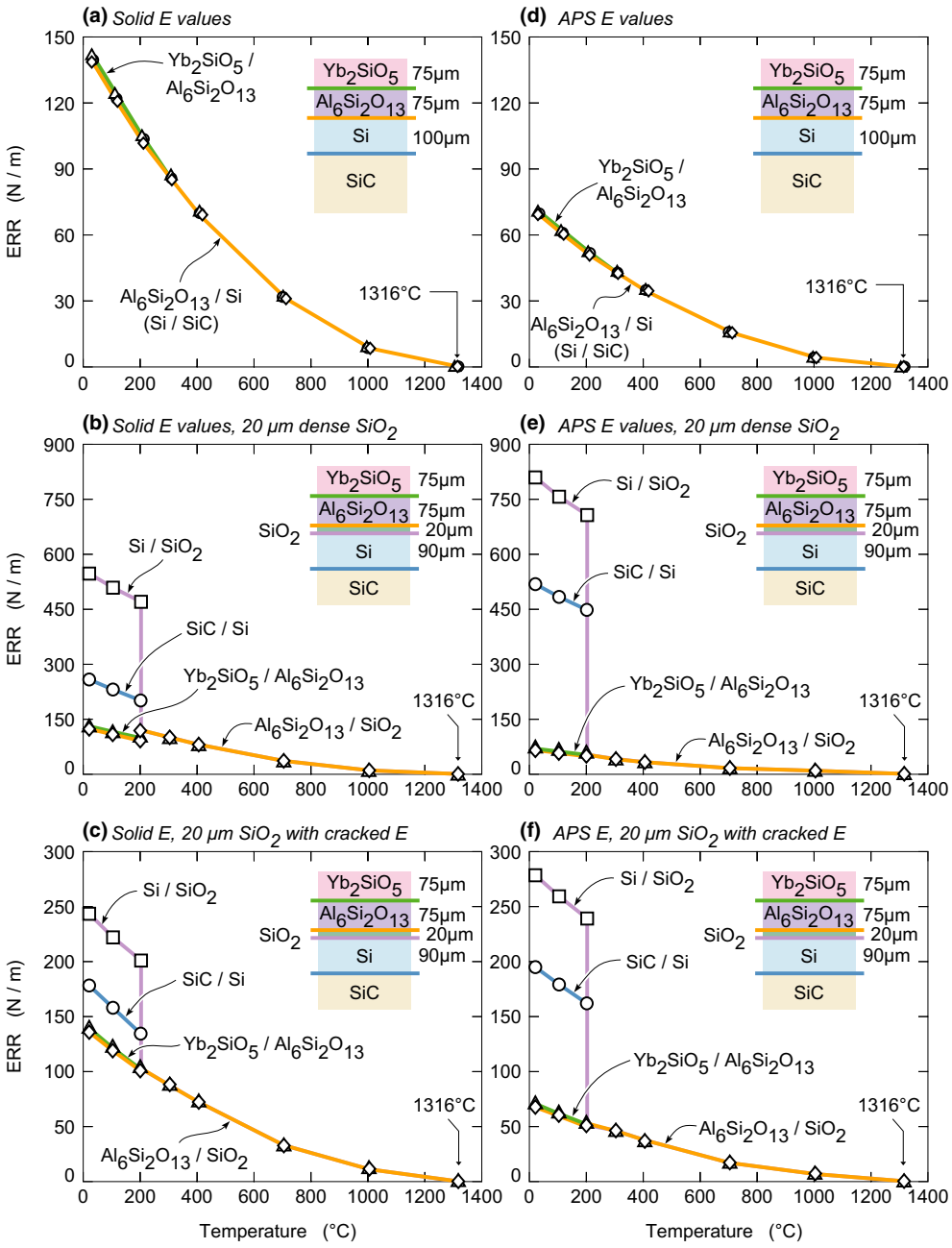

Fig. 12. The stored elastic energy release rate for delamination at the various interfaces of a tri-layer EBC as a function of temperature. (a) Annealed coating assuming bulk elastic moduli, (b) the same coating after growing a 20-μm-thick cristobalite TGO at the $Al_6Si_2O_{13}$–Si interface, and (c) the same scenario in (b) but with a 50% reduced TGO elastic modulus. (d), (e), and (f) repeat (a), (b), and (c) but with the reduced elastic moduli (for APS materials) given in Table I.

Upon cooling, Fig. 13(c), the CTE mismatch-derived residual stresses began to develop and the mud cracks began to reopen. Significant bending moments are expected (based on elastic analyses) because the CTE of coating layers decreased progressively from the topcoat down. As the TGO grown on the bond coat thickened with increasing high-temperature exposure time, the available driving force for mechanical damage rapidly became dominated by the release of strain energy in the TGO, as indicated in Fig. 12. During cooling, the thermally grown β cristobalite transformed to the α-phase at around 220°C with a volume reduction of ~4.5%. This volume change was constrained by adhesion to the surrounding layers, resulting in microcracking of the TGO. During the next heating cycle, the TGO microcrack network provided a fast diffusion path for O_2 and steam to reach un-oxidized Si, increasing the oxidation rate. Repeated thermal cycling resulted in rapid growth of the TGO and eventual linkage of the TGO regions emanated from each mud crack.

Delamination was initiated at the edge of the coatings, where the severity of the damage mechanisms shown in Figs. 13(a)–(c) was increased due to more severe environmental attack, Fig. 13(d). Even though attempts were made to wrap the Yb_2SiO_5 and $Al_6Si_2O_{13}$ layers around the edge of the substrate, the Si bond coat was left unprotected at the sample edge. This resulted in rapid oxide growth both on and within the bond coat (the latter due to the presence of an interconnected pore network). Upon cooling, TGO microcracking commenced and this enabled more rapid oxidizer penetration and TGO formation during subsequent hot cycles. The large bending moment and substantial ERR that was developed upon cooling resulted in release of the coating segment between the edge and the first mud crack, with further cycling progressively extending this mode of coating delamination.

It is evident that the rapid delamination failure of the tri-layer coating system was controlled by the high diffusivity

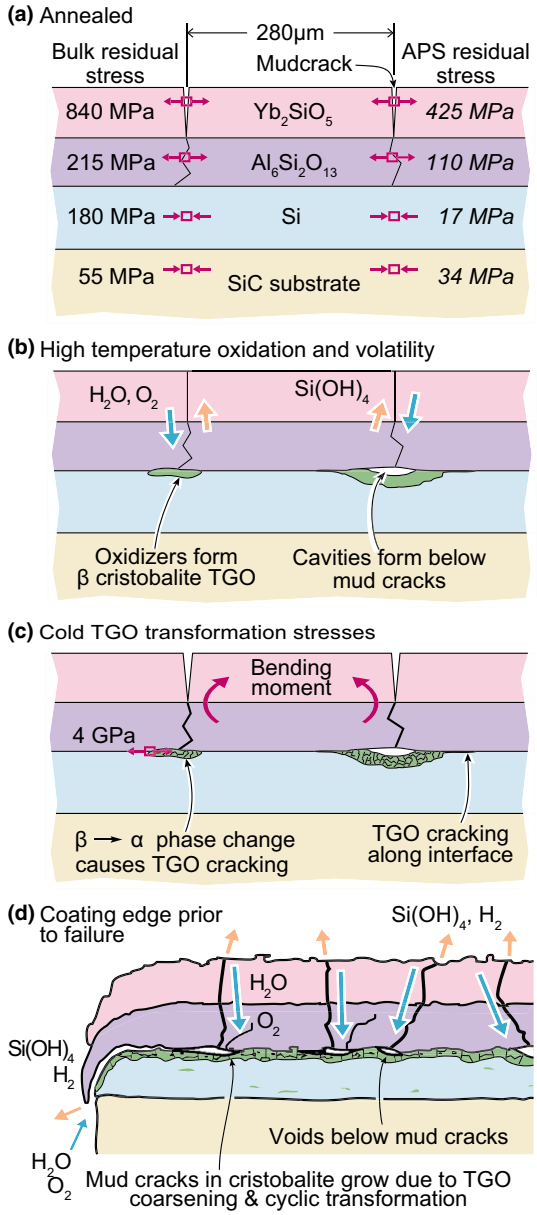

Fig. 13. The damage mechanism sequence in an Yb_2SiO_5/$Al_6Si_2O_{13}$/Si tri-layer EBC applied to an α-SiC substrate. (a) Shows the initial damage and stress states in the annealed EBC, (b) shows the TGO reaction at 1316°C and (c) details mechanical damage upon cooling to low temperature. (d) Shows a schematic illustration of the edge damage and failure mechanism.

pathways for oxidation and silica volatilization at either the coating edges or the mud cracked Yb_2SiO_5 and $Al_6Si_2O_{13}$ layers. Future coating developments should be focused upon systems where exposed edges are avoided and where the CTE mismatch between the layers of the coating and the substrate is sufficiently small to avoid mud crack formation. This CTE matching constraint in combination with the need for low silica activity will significantly reduce the number of candidate coating materials. The study has also identified two vulnerabilities of the Si bond coat. First, it is essential to identify optimized deposition conditions that produce a dense Si coating that does not contain surface connected pores. Second, the formation of a *cristobalite TGO* and its high stored elastic strain energy upon cooling will be problematic for practical EBC systems. Oxidizing species will eventually diffuse through the outer layers of the EBC and lead to the formation of a TGO at the silicon surface. If the formation of cristobalite can be slowed or avoided, the driving force for delamination could be reduced and the coating lifetime might be considerably extended.

VI. Conclusions

Three-layer Yb_2SiO_5/$Al_6Si_2O_{13}$/Si EBCs have been deposited onto SiC substrates using an APS approach. These coatings have been steam cycled to failure (defined as any observed spallation) in an atmospheric pressure, slowly flowing 90% H_2O/10% O_2 environment using 60 min hot (1316°C) and 10 min cool (110°C) cycles. The coating lifetime was controlled by interactions between environmental degradation and mechanical damage resulting from thermal residual stresses and phase transformation. Specifically, it is found that:

1. Mud cracking of the as-deposited and annealed EBC was indicative of a thermomechanical incompatibility in the system. This led to the development of short circuit diffusion/volatilization paths through the water vapor protective layers of the EBC.
2. Oxygen and steam penetrate through the upper layers of the EBC and oxidize the Si bond coat. The dominant oxidizer access route appears to be through mud cracks and eroded channels in the TGO. The high testing temperature of 1316°C resulted in the formation of β (high) cristobalite as opposed to vitreous SiO_2.
3. Thermally grown cristobalite experiences a phase transformation upon cooling at around 220°C that is accompanied by considerable volumetric contraction. This caused severe fracturing of the TGO, and ultimately led to coating delamination. *The formation of a cristobalite TGO was a major contributing factor to the poor steam cycling durability of this tri-layer EBC system.*

Acknowledgments

We would like to acknowledge Bryan Harder, Dennis Fox, and Michael Cuy of the NASA Glenn Research Center for their assistance in depositing EBCs. The authors are indebted to Stephen Sehr (UCSB) and Foucault de Franqville (Cachan) for help with the energy release rate calculations in this work. We thank Elizabeth Opila (UVA), Dongming Zhu of NASA Glenn and Kang Lee from Rolls Royce (Indianapolis) for numerous helpful discussions. We would also like to thank Richard White (UVA) for advice concerning coating characterization. This work was supported in part by Rolls Royce (Indianapolis) and the Office of Naval Research under grants N00014-11-1-0917 (BTR and HNGW) and N00014-13-1-0859 (MRB) managed by Dr. David Shifler.

References

[1]M. P. Boyce, *Gas Turbine Engineering Handbook*. Butterworth-Heinemann, Oxford, UK (2011).
[2]T. Giampaolo, *The Gas Turbine Handbook: Principles and Practices*. The Fairmont Press, Lilburn, Georgia, 2003.
[3]P. P. Walsh and P. Fletcher, *Gas Turbine Performance*. Blackwell Science Limited, Fairfield, NJ, 2004.
[4]J. H. Perepezko, "The Hotter the Engine, the Better," *Science*, **326** [5956] 1068–9 (2009).
[5]A. G. Evans, F. W. Zok, and J. Davis, "The Role of Interfaces in Fiber-Reinforced Brittle Matrix Composites," *Compos. Sci. Technol.*, **42** [1–3] 3–24 (1991).
[6]M. Rühle and A. G. Evans, "High Toughness Ceramics and Ceramic Composites," *Prog. Mater Sci.*, **33** [2] 85–167 (1989).
[7]D. B. Marshall and A. G. Evans, "Failure Mechanisms in Ceramic-Fiber/Ceramic-Matrix Composites," *J. Am. Ceram. Soc.*, **68** [5] 225–31 (1985).
[8]A. G. Evans and D. B. Marshall, "Overview No. 85 The Mechanical Behavior of Ceramic Matrix Composites," *Acta Metall.*, **37** [10] 2567–83 (1989).
[9]J. DiCarlo, H.-M. Yun, G. Morscher, and R. Bhatt, "SiC/SiC Composites for 1200°C and Above"; pp. 77–98 in *Handbook of Ceramic Composites*, Edited by N. P. Bansal. Kluwer Academic Publishers, New York, 2005.
[10]S. Zhu, M. Mizuno, Y. Nagano, J. Cao, Y. Kagawa, and H. Kaya, "Creep and Fatigue Behavior in an Enhanced SiC/SiC Composite at High Temperature," *J. Am. Ceram. Soc.*, **81** [9] 2269–77 (1998).
[11]G. N. Morscher, et al., "Tensile Creep and Fatigue of Sylramic-iBN Melt-Infiltrated SiC Matrix Composites: Retained Properties, Damage Development, and Failure Mechanisms," *Compos. Sci. Technol.*, **68** [15–16] 3305–13 (2008).
[12]E. J. Opila, "Variation of the Oxidation Rate of Silicon Carbide with Water-Vapor Pressure," *J. Am. Ceram. Soc.*, **82**, 625–36 (1999).

[13]E. J. Opila, "Oxidation and Volatilization of Silica Formers in Water Vapor," *J. Am. Ceram. Soc.*, **86**, 1238–48 (2003).
[14]E. J. Opila, D. S. Fox, and N. S. Jacobson, "Mass Spectrometric Identification of Si-O-H(g) Species from the Reaction of Silica with Water Vapor at Atmospheric Pressure," *J. Am. Ceram. Soc.*, **80**, 1009–12 (1997).
[15]E. J. Opila and R. E. Hann Jr., "Paralinear Oxidation of CVD SiC in Water Vapor," *J. Am. Ceram. Soc.*, **80**, 197–205 (1997).
[16]E. J. Opila, J. L. Smialek, R. C. Robinson, D. S. Fox, and N. S. Jacobson, "SiC Recession Caused by SiO_2 Scale Volatility Under Combustion Conditions: II, Thermodynamics and Gaseous-Diffusion Model," *J. Am. Ceram. Soc.*, **82**, 1826–34 (1999).
[17]B. N. Cox and F. W. Zok, "Advances in Ceramic Composites Reinforced by Continuous Fibers," *Curr. Opin. Solid State Mater. Sci.*, **1** [5] 666–73 (1996).
[18]F. E. Heredia, J. C. McNulty, F. W. Zok, and A. G. Evans, "Oxidation Embrittlement Probe for Ceramic-Matrix Composites," *J. Am. Ceram. Soc.*, **78** [8] 2097–100 (1995).
[19]T. E. Steyer, F. W. Zok, and D. P. Walls, "Stress Rupture of an Enhanced Nicalon/Silicon Carbide Composite at Intermediate Temperatures," *J. Am. Ceram. Soc.*, **81** [8] 2140–6 (1998).
[20]L. U. Ogbuji, "Pest-Resistance in SiC/BN/SiC Composites," *J. Eur. Ceram. Soc.*, **23** [4] 613–7 (2003).
[21]L. U. J. T. Ogbuji, "Oxidative Pest Degradation of Hi-Nicalon/BN/SiC Composite as a Function of Temperature and Time in the Burner Rig"; pp. 105–114 in *23nd Annual Conference on Composites, Advanced Ceramics, Materials, and Structures-B: Ceramic Engineering and Science Proceedings*, Vol. 230, Edited by E. Ustundag and G. Fischman American Ceramics Society, Westerville, OH, 1999.
[22]K. J. LaRochelle and G. Morscher, "Tensile Stress Rupture Behavior of a Woven Ceramic Matrix Composite in Humid Environments at Intermediate Temperature—Part I," *Appl. Compos. Mater.*, **13** [3] 147–72 (2006).
[23]K. N. Lee, D. S. Fox, and N. P. Bansal, "Rare Earth Silicate Environmental Barrier Coatings for SiC/SiC Composites and Si_3N_4 Ceramics," *Corrosion of Ceramic Matrix Composites*, **25**, 1705–15 (2005).
[24]K. N. Lee, N. S. Jacobson, and R. A. Miller, "Refractory Oxide Coatings on SiC Ceramics," *MRS Bull.*, **19**, 35–8 (1994).
[25]K. N. Lee, "Current Status of Environmental Barrier Coatings for Si-Based Ceramics," *Surf. Coat. Technol.*, **133–134**, 1–7 (2000).
[26]K. N. Lee, "Key Durability Issues with Mullite-Based Environmental Barrier Coatings for Si-Based Ceramics," *J. Eng. Gas Turbines Power*, **122**, 632–6 (2000).
[27]K. N. Lee, "Protective Coatings for Gas Turbines"; pp. 431 in *The Gas Turbine Handbook*, Section 4.4.2, U.S. Department of Energy, NETL, 2006.
[28]K. N. Lee, J. I. Eldridge, and R. C. Robinson, "Residual Stresses and Their Effects on the Durability of Environmental Barrier Coatings for SiC Ceramics," *J. Am. Ceram. Soc.*, **88**, 3483–8 (2005).
[29]K. N. Lee, et al., "Upper Temperature Limit of Environmental Barrier Coatings Based on Mullite and BSAS," *J. Am. Ceram. Soc.*, **86**, 1299–306 (2003).
[30]K. N. Lee and R. A. Miller, "Development and Environmental Durability of Mullite and Mullite/YSZ Dual Layer Coatings for SiC and Si_3N_4 Ceramics," *Surf. Coat. Technol.*, **86–87**, 142–8 (1996).
[31]B. T. Richards and H. N. G. Wadley, "Plasma Spray Deposition of Tri-Layer Environmental Barrier Coatings," *J. Eur. Ceram. Soc.*, **34** [12] 3069–83 (2014).
[32]N. S. Jacobson, D. S. Fox, J. L. Smialek, E. J. Opila, C. Dellacorte and K. N. Lee, "Performance of Ceramics in Severe Environments"; pp. 565–78 in *ASM Handbook* Vol. 13B, Corrosion: Materials. ASM International, Materials Park, OH, 2005.
[33]K. N. Lee, "Contamination Effects on Interfacial Porosity During Cyclic Oxidation of Mullite-Coated Silicon Carbide," *J. Am. Ceram. Soc.*, **81**, 3329–32 (1998).
[34]K. N. Lee and R. A. Miller, "Oxidation Behavior of MuIlite-Coated SiC and SiC/SiC Composites Under Thermal Cycling Between Room Temperature and 1200°C-1400°C," *J. Am. Ceram. Soc.*, **79**, 620–6 (1996).
[35]D. Zhu, S. R. Choi, J. I. Eldridge, K. N. Lee, and R. A. Miller, "Surface Cracking and Interface Reaction Associated Delamination Failure of Thermal and Environmental Barrier Coatings," Symposium on Advanced Ceramic Coatings for Structural, Environmental and Functional Applications 27th Annual International Conference on Advanced Ceramics and Composites. 26–31 January Cocoa Beach, FL, 2005. NASA NTRS 20050212126
[36]D. Zhu, K. N. Lee, and R. A. Miller, "Thermal Gradient Cyclic Behavior of a Thermal/Environmental Barrier Coating System on SiC/SiC Ceramic Matrix Composites"; pp. 171–8 in *ASME Turbo Expo 2002: Power for Land, Sea, and Air*, Vol. 4: Parts A and B, June 3–6, Amsterdam, The Netherlands, 2002.
[37]D. Zhu, K. N. Lee, and R. A. Miller, "Cyclic Failure Mechanisms of Thermal and Environmental Barrier Coating Systems Under Thermal Gradient Test Conditions," NASA/TM-2002-211478, (2002).
[38]R. W. Jackson and M. R. Begley, "Critical Cooling Rates to Avoid Transient-Driven Cracking in Thermal Barrier Coating (TBC) Systems," *Int. J. Solids Struct.*, **51** [6] 1364–74 (2014).
[39]Z. Sun, Y. Zhou, J. Wang, and M. Li, "Γ-$Y_2Si_2O_7$, a Machinable Silicate Ceramic: Mechanical Properties and Machinability," *J. Am. Ceram. Soc.*, **90** [8] 2535–41 (2007).
[40]D. Lakshtanov, S. Sinogeikin, and J. Bass, "High-Temperature Phase Transitions and Elasticity of Silica Polymorphs," *Phys Chem Minerals*, **34** [1] 11–22 (2007).
[41]K. N. Lee, R. A. Miller, and N. S. Jacobson, "New Generation of Plasma-Sprayed Mullite Coatings on Silicon Carbide," *J. Am. Ceram. Soc.*, **78**, 705–10 (1995).
[42]H. Ledbetter, S. Kim, D. Balzar, S. Crudele, and W. Kriven, "Elastic Properties of Mullite," *J. Am. Ceram. Soc.*, **81**, 1025–8 (1998).
[43]T.-I. Mah and K. S. Mazdiyasni, "Mechanical Properties of Mullite," *J. Am. Ceram. Soc.*, **66**, 699–703 (1983).
[44]D. R. Peacor, "High-Temperature Single-Crystal Study of the Cristobalite Inversion," *Z. Kristallogr.*, **138**, 274–98 (1973).
[45]K. Yamahara, K. Okazaki, and K. Kawamura, "Molecular Dynamics Study of the Thermal Behaviour of Silica Glass/Melt and Cristobalite," *J. Non-Cryst. Solids*, **291** [1–2] 32–42 (2001).
[46]H. Gercek, "Poisson's Ratio Values for Rocks," *Int. J. Rock Mech. Min. Sci.*, **44** [1] 1–13 (2007).
[47]E. Bourova and P. Richet, "Quartz and Cristobalite: High-Temperature Cell Parameters and Volumes of Fusion," *Geophys. Res. Lett.*, **25** [13] 2333–6 (1998).
[48]A. Ballato, "Poisson's Ratios of Auxetic and Other Technological Materials," *Ultrasonics, Ferroelectrics and Frequency Control, IEEE Transactions on*, **57** [1] 7–15 (2010).
[49]R. Hull, *Properties of Crystalline Silicon*. The Institution of Engineering and Technology, London (1999).
[50]T. A. Cruse, B. Johnsen, and A. Nagy, "Mechanical Properties Testing and Results for Thermal Barrier Coatings," *J Therm Spray Tech*, **6** [1] 57–66 (1997).
[51]J. T. Demasi and M. Ortiz, "Thermal Barrier Coating Life Prediction Model Development, Phase 1," NASA Contractor Report 182230 (1989).
[52]S.-H. Leigh, C.-K. Lin, and C. C. Berndt, "Elastic Response of Thermal Spray Deposits Under Indentation Tests," *J. Am. Ceram. Soc.*, **80** [8] 2093–9 (1997).
[53]C. J. Li and A. Ohmori, "Relationships Between the Microstructure and Properties of Thermally Sprayed Deposits," *J Therm Spray Tech*, **11** [3] 365–74 (2002).
[54]S. M. Meier, D. M. Nissley, K. D. Sheffler, and T. A. Cruse, "Thermal Barrier Coating Life Prediction Model Development," *J. Eng. Gas Turbines Power*, **114** [2] 258–63 (1992).
[55]B. T. Richards, L. J. Ghosn, D. Zhu, and H. Wadley, "Mechanical Properties of Air Plasma Sprayed Environmental Barrier Coating (EBC) Systems: Preliminary Assessments"; Proceedings of the 39th International Conference and Exposition on Advanced Ceramics and Composites. 25–30 January, 2015, Daytona Beach, Fl (in press).
[56]S. R. Choi, D. Zhu, and R. A. Miller, "Mechanical Properties/Database of Plasma-Sprayed ZrO_2-8wt% Y_2O_3 Thermal Barrier Coatings," *Int. J. Appl. Ceram. Technol.*, **1** [4] 330–42 (2004).
[57]J. S. Wallace and J. Ilavsky, "Elastic Modulus Measurements in Plasma Sprayed Deposits," *J Therm Spray Tech*, **7** [4] 521–6 (1998).
[58]C. Li, A. Ohmori, and R. McPherson, "The Relationship Between Microstructure and Young's Modulus of Thermally Sprayed Ceramic Coatings," *J. Mater. Sci.*, **32** [4] 997–1004 (1997).
[59]J. B. Bates, "Raman Spectra of α and β Cristobalite," *J. Chem. Phys.*, **57** [9] 4042–7 (1972).
[60]F. L. Galeener, "Raman and ESR Studies of the Thermal History of Amorphous SiO_2," *J. Non-Cryst. Solids*, **71** [1–3] 373–86 (1985).
[61]I. P. Swainson, M. T. Dove, and D. C. Palmer, "Infrared and Raman Spectroscopy Studies of the α–B Phase Transition in Cristobalite," *Phys Chem Minerals*, **30** [6] 353–65 (2003).
[62]D. Hatch and S. Ghose, "The α-β Phase Transition in Cristobalite, SiO_2," *Phys Chem Minerals*, **17** [6] 554–62 (1991).
[63]A. J. Leadbetter and A. F. Wright, "The α—B Transition in the Cristobalite Phases of SiO_2 and $AlPO_4$ I. X-ray Studies," *Phil. Mag.*, **33** [1] 105–12 (1976).
[64]G. H. A. M. van der Steen and H. van den Boom, "Raman Spectroscopic Study of Hydrogen-Containing Vitreous Silica," *J. Non-Cryst. Solids*, **23** [2] 279–86 (1977).
[65]D. Tromans and J. A. Meech, "Fracture Toughness and Surface Energies of Minerals: Theoretical Estimates for Oxides, Sulphides, Silicates and Halides," *Miner. Eng.*, **15** [12] 1027–41 (2002).
[66]L. B. Freund and S. Suresh, *Thin Film Materials: Stress, Defect Formation, and Surface Evolution*, pp. 750. Cambridge University Press, Cambridge, UK, 2003.
[67]K. L. More, P. F. Tortorelli, M. K. Ferber, and J. R. Keiser, "Observations of Accelerated Silicon Carbide Recession by Oxidation at High Water-Vapor Pressures," *J. Am. Ceram. Soc.*, **83** [1] 211–3 (2000).
[68]P. F. Tortorelli and K. L. More, "Effects of High Water-Vapor Pressure on Oxidation of Silicon Carbide at 1200°C," *J. Am. Ceram. Soc.*, **86** [8] 1249–55 (2003). □